

Improved thermoelectric properties in directionally grown $\text{Bi}_2\text{Sr}_2\text{Co}_{1.8}\text{O}_y$ ceramics by Pb for Bi substitution

A. Sotelo¹, Sh. Rasekh¹, E. Guilmeau², M. A. Madre¹, M. A. Torres³, S. Marinel², J. C. Diez¹

¹Instituto de Ciencia de Materiales de Aragón (CSIC-Universidad de Zaragoza), M^a de Luna 3, 50018 Zaragoza, Spain.

² CRISMAT Laboratory, UMR 6508 CNRS-ENSICAEN, 6 Bld. Maréchal Juin, 14050 Caen cedex (France).

³ Departamento de Ingeniería de Diseño y Fabricación. Universidad de Zaragoza, M^a de Luna, 3. 50018 Zaragoza, Spain.

Abstract

Thermoelectric performances of misfit cobaltites can be controlled by grain orientation and/or by cation substitution. Both processes have been simultaneously performed by directional solidification at 0.03 m/h, using the laser floating zone technique, of $\text{Bi}_{2-x}\text{Pb}_x\text{Sr}_2\text{Co}_{1.8}\text{O}_y$ (with $x = 0.0, 0.2, 0.4$ and 0.6). The microstructure has shown two different main phases as a function of Pb content, a Co-poor phase for low Pb content (0.0 and 0.2) and a Co-rich one for higher Pb substitution. These microstructural changes are reflected on the thermoelectric properties leading to an important decrease on the resistivity and increase of thermopower for samples with 0.4Pb substitution. Both improvements lead to power factor values higher than usual in textured misfit cobaltites.

Keywords: A. Ceramics, A. Oxides; B. Electrical properties

Corresponding author: Juan Carlos Diez

e-mail: monux@unizar.es

Address: Dept. Ciencia de Materiales; C/M^a de Luna, 3; 50018-Zaragoza; Spain

Tel: +34 976762526

Fax: +34 976761957

1. Introduction

Thermoelectric (TE) materials with high energy conversion efficiency are strongly required for both electric power generation, in terms of waste heat recovery, and refrigeration. Thermoelectric energy conversion has been shown as an effective technology that can be used to transform thermal to electrical energy owing to the well-known Seebeck effect. This physical property allows producing electrical power from a thermal gradient between the cold and the hot side of a thermoelectric system. The conversion efficiency of such materials is usually quantified by the dimensionless figure of merit ZT , which is defined as $TS^2/\rho\kappa$, where S is the Seebeck coefficient (or thermopower), ρ the electrical resistivity, κ the thermal conductivity, and T is the absolute temperature [1]. As a consequence, a performant TE material involves high thermopower and low resistivity, with low thermal conductivity.

From 1997, with the discovery of large thermoelectrical properties in Na_xCoO_2 [2], great efforts have been performed to explore new CoO families with high thermoelectric performances. Following this intense research work, some layered cobaltites, such as $[\text{Ca}_2\text{CoO}_3][\text{CoO}_2]_{1.62}$ and $[\text{Bi}_{0.87}\text{SrO}_2]_2[\text{CoO}_2]_{1.82}$ were also found to exhibit good thermoelectric properties [3-6]. Moreover, these materials can operate at high temperature in air without degradation, as compared to the intermetallic thermoelectric compounds, which is other way of improving the ZT values.

The crystal structure of these CoO families is composed of two different layers, with an alternate stacking of a common conductive CdI_2 -type CoO_2 layer with a two-dimensional triangular lattice and a block layer, composed of insulating rock-salt-type (RS) layers. The two sublattices (RS block and CdI_2 -type CoO_2

layer) possess common *a*- and *c*-axis lattice parameters and β angles but different *b*-axis length, causing a misfit along the *b*-direction [7-9].

As layered cobaltites are materials with a strong crystallographical anisotropy, the alignment of plate-like grains by mechanical and/or chemical processes is necessary to attain macroscopic properties comparable to those obtained on single crystals. Some techniques have been shown to be adequate to obtain a good grain orientation in several oxide ceramic systems, as Template Grain Growth (TTG) [9], sinter-forging [10], or directional growth from the melt [11]. On the other hand, it is interesting to explore cationic substitution in the RS layer, changing the misfit relationship between the two layers and, as a consequence, tuning up the values of the thermopower [6]. From this point of view, it is clear that this substitution can be useful in order to improve thermoelectric performances of ceramic materials [10], as it is reported for the substitution of Gd and Y for Ca [12], or Pb for Bi [13].

The aim of the present work is studying the effect of the Pb for Bi substitution, in different proportions, on the microstructure and thermoelectric properties of directionally grown ceramics from the melt using the laser floating zone (LFZ) technique.

2. Experimental

The polycrystalline $\text{Bi}_{2-x}\text{Pb}_x\text{Sr}_2\text{Co}_{1.8}\text{O}_y$ (with $x = 0, 0.2, 0.4, \text{ and } 0.6$) ceramic powders used in this study have been prepared by the classical solid state route from commercial Bi_2O_3 (Panreac, 98 + %), SrCO_3 (Panreac, 98 + %), Co_2O_3 (Aldrich, 98 + %), and PbO (Aldrich, ≥ 99 %) powders. They were weighed in the appropriate proportions, mixed and ball milled at 300 rpm for 30 minutes to

obtain a homogeneous mixture. This powder has then been thermally treated twice at 1020 and 1080K for about 12 hours under air, with an intermediate manual milling, in order to assure the complete decomposition of the carbonates. Otherwise, the presence of carbonates would form CO₂ bubbles in the molten zone produced in the LFZ process which can produce the crystallization front destabilization. The resulting powders were then cold isostatically pressed at ~200 MPa to obtain green ceramic cylinders which were subsequently used as feed in a LFZ device [14] equipped with a continuous power Nd:YAG laser ($\lambda = 1.06 \mu\text{m}$). The processing of the different samples has been performed in the same conditions; they were directionally crystallized downwards from the melt at 0.03 m/h with a seed rotation of 3 rpm. Moreover, in order to assure compositional homogeneity of the molten zone, an opposite feed rotation of 15 rpm has also been performed. Finally, after the texturing process, long (more than 0.15 m) and geometrically homogeneous (~0.002 m diameter) textured cylindrical rods have been produced.

The identification of the main phases in all textured samples was carried out using powder XRD in a Rigaku D/max-B X-ray powder diffractometer (CuK α radiation), between 10 and 70°, using Si as reference. Microstructures have been observed using a scanning electron microscope (JEOL 6000) equipped with an energy dispersive spectroscopy (EDS) device, used to determine the elemental composition of each phase. Micrographs of longitudinal fractured sections have been recorded to determine the grain orientation. Transversal polished sections of the textured phases have been observed to analyze the different phases and their distribution. Image analysis has been performed on several transversal micrographs for each composition in order to estimate the

volume fraction of each phase. Longitudinal polished sections of each sample have been used to estimate the proportion of the different phases. Electrical resistivity (ρ) and thermopower (S) were simultaneously determined by the standard dc four-probe technique in a ZEM-3 measurement system (Ulvac-Riko), in the steady state mode, at temperatures ranging from 300 to 925K. With the electrical resistivity and thermopower data, the power factor (PF) has been calculated ($PF = S^2/\rho$) in order to determine the samples performances.

3. Results and discussion

Powder XRD patterns for the different $\text{Bi}_{2-x}\text{Pb}_x\text{Sr}_2\text{Co}_{1.8}\text{O}_y$ samples (from 10 to 35 degrees, for clarity) are displayed in Fig. 1. From these data, it is clear that all the samples have very similar diffraction patterns and show a very low amount of secondary phases. The highest peaks belong to the misfit cobaltite phase and are in agreement with previously reported data [13]. Weak diffraction peak at about 29 degrees (marked with a *) is related to the (Bi,Pb)-Sr-O secondary phase [15]. The weakest peaks, indicated by # could not be identified. As it can be seen in Fig. 1, the cobaltite and (Bi,Pb)-Sr-O peaks show a significative displacement towards lower angles when Pb for Bi substitution is increased while there is no displacement for the peaks marked with #. The peaks displacement to lower 2θ angles is due to the modification of the cell parameters. For the cobaltite phase, this modification is produced in the RS layer which contents the Bi^{+3} cations. In order to evaluate the c parameter relative variation as a function of the Pb content, the (0010) diffraction peaks (represented in Fig. 2) have been used. The modification of the c -parameter is represented in the insert of Fig. 2 which evidences a linear relationship between

the nominal Pb content and the *c*-parameter until a maximum Pb solubility in the samples is reached for nominal 0.4Pb contents. Higher nominal Pb addition does not seem to increase its content into the crystal structure.

A representative micrograph, performed on longitudinal fractured samples, is shown in Fig. 3. This micrograph illustrates the good orientation of the plate-like grains and their size, exceeding easily 100 μm in the *ab* plane, while they are very thin in the *c*-direction. On the other hand, these plate-like grains are composed, in turn, by many thin and well stacked grains. In order to evaluate the *c*-dimension of each individual grain, X-ray line broadening measurements were performed, obtaining an approximate thickness of about 0.4 μm in all cases.

The microstructural evolution of samples, as a function of the Pb content can be easily observed in Fig. 4 that shows the transversal and longitudinal polished sections of all samples, and Table I, where the different phases and their amount in each sample are summarized. In Fig. 4a it can be observed the transversal surface of the Pb-free sample which is formed by five different phases, each one identified by EDS analysis (see Table I) and corresponding to a different contrast (numbered in Fig. 4a for clarity). As it can be clearly seen in Table I, Pb addition leads to the disappearing of CoO (black contrast) and the reduction of the amount and size of Sr-Co-O phase (dark grey contrast), independently of the Pb amount. Other microstructural changes are produced as a function of Pb content: 0.2Pb addition produces a slight increase of the thermoelectric phase, with a composition close to the 222 phase (grey contrast), where all the added Pb is incorporated. Increasing nominal Pb content to 0.4 has produced a drastic change in the microstructure: Bi-Sr-Co-O phase, with

composition close to the 221 one, disappears leading to a spectacular increase of the thermoelectric 222 phase volume (from around 26% for the 0.2Pb samples to 83% for the 0.4Pb ones) and a slighter raise of (Bi,Pb)-Sr-O phase, identified as white contrast (from about 2% for the 0.2Pb samples to 13% for the 0.4Pb ones). In these samples, Pb substitution is not only produced in the 222 thermoelectric phase, but also in the (Bi,Pb)-Sr-O one. Further Pb addition to 0.6 reduces the amount of the thermoelectric 222 phase and increases the secondary (Bi,Pb)-Sr-O phase content. Moreover, the increase of Pb content does not change its amount in the thermoelectric 222 phase which has reached the maximum Pb solubility. As a consequence, this additional Pb amount is only substituting Bi in the (Bi,Pb)-Sr-O, explaining not only the higher content of this phase in the 0.6Pb samples, but also the higher peak (marked with a * in Fig.1) displacement observed in the XRD plot. On the other hand, dark grey phase is found in all samples with very similar composition and very low amounts, indicating that the unindexed XRD peaks probably correspond to this phase while the reduction of their intensity with the increase of the Pb content can be associated to the refinement of the grain size observed when Pb is added. Fig. 4e-h shows the longitudinal polished sections of all samples where the microstructural evolution described above is confirmed. On the other hand, new features can be found in these micrographs. In Fig. 4e, it is clear that the sample can be described, approximately, as a light grey matrix where the rest of the phases are included. Samples with 0.2Pb addition nearly maintains the main phases amount (222 and 221 phases), but changes drastically the phases shape and their orientation. Samples are now composed of thin (compared with the undoped samples) alternate grains of both main phases with the secondary

phases (dark grey and white contrasts) as inclusions. Further Pb content increases the 222 and Sr-Co-O amount while the 221 phase disappears, leading to samples formed by a 222 matrix and secondary phases as inclusions. The proportion of secondary phases is lower for samples with 0.4Pb than for the 0.6Pb ones as discussed in Fig. 4.

In order to study the effect of Pb on the thermoelectrical properties of this ceramic family, the temperature dependence of the electrical resistivity, as a function of the Pb content, has been measured and represented in Fig. 5. As it can be easily seen, undoped and 0.2 samples possess very similar behaviour, while higher Pb content ones display a different one. The first group of samples (0.0 and 0.2Pb) show semiconducting-like properties in the whole range of temperatures and the second one (0.4 and 0.6Pb), semiconducting-like behaviour from room temperature to about 725K and metallic-like from 725 to 925K. The different behaviour of both groups can be explained by the microstructural features described above. For the undoped sample, the main conducting phase is the 221 (light grey contrast in Fig. 4) which forms a continuous matrix along the samples and is responsible for the high resistivity values measured. The addition of 0.2Pb increases resistivity values, compared with the undoped samples, despite of the higher amount of 222 phase found in 0.2Pb ones. In order to explain this apparently contradictory behaviour, it is necessary to observe carefully the microstructural features shown in Fig. 4f. As it can be clearly observed, samples are now composed by thin alternate grains of the 222 and 221 phases. Moreover, they do not form a continuous path for the electrical conduction. As a consequence, the increase on the resistivity for the 0.2Pb samples can be probably associated to the high resistivity of the grain

boundaries between the 221 and 222 phases. Moreover, Pb addition produces hole doping due to the Pb^{2+} substitution for Bi^{3+} which induce the oxidation of Co^{+3} to Co^{+4} in the conducting layer as well as promoting the incorporation of higher Co amount in the structure [6] and, as a consequence, reducing the electrical resistivity [16]. On the other hand, the increase in the resistivity values for the 0.6Pb doped samples is related to the raise of secondary phases proportion. The minimum resistivity value ($1.7 \cdot 10^{-4} \Omega\cdot\text{m}$) at about 300K is obtained for the 0.4Pb doped sample, around the best reported values for this type of materials [10,16].

Fig. 6 displays the variation of thermopower with temperature, as a function of the Pb content. It can be clearly seen that the sign of the thermopower is positive for the entire measured temperature range for all compositions which confirms a conduction governed by holes. The graph shows a different behaviour, from high (0.4 and 0.6) to low Pb content samples (0.0 and 0.2), as observed for the resistivity measurements and confirming the effect of the microstructural changes on the thermoelectrical properties. The variable behaviours in the temperature dependence of the Seebeck coefficient curves can be originated by the large amounts of secondary phases. In the case of undoped and 0.2Pb doped samples, it is observed a reduction of thermopower from room temperature to around 725K, followed by a small increase at higher temperatures. The highly doped samples (0.4 and 0.6Pb) show a decrease on the thermopower values until about 425K, but higher temperatures produce an important increase, reaching a maximum value of about $1.4 \cdot 10^{-4} \text{ V/K}$ at 925K for the 0.4Pb samples. In all cases, the measured thermopower values at room temperature are higher than those reported in the literature [9,10]. These high

values are in apparently contradiction with the previously discussed electrical resistivity evolution in a broad band model. However, it can be explained by a narrow band model already used for Bi(Pb)-Sr-Co-O solid state sintered specimens [16].

In order to evaluate the thermoelectric performances of these materials, PF has been calculated from the resistivity and thermopower values and plotted in Fig. 7. When considering PF values at about 300K (~room temperature), it can be clearly seen that undoped samples, as well as 0.2Pb doped ones, have the same values (around $0.5 \cdot 10^{-4} \text{ W/K}^2\text{m}$), followed by an important increase for the 0.4Pb doped samples, reaching $1.0 \cdot 10^{-4} \text{ W/K}^2\text{m}$ and decreasing for further Pb addition to about $0.7 \cdot 10^{-4} \text{ W/K}^2\text{m}$. This maximum value is higher than the obtained for textured materials reported in the literature (around $0.8 \cdot 10^{-4} \text{ W/K}^2\text{m}$) [10].

4. Conclusions

This paper demonstrates that $\text{Bi}_{2-x}\text{Pb}_x\text{Sr}_2\text{Co}_{1.8}\text{O}_y$ thermoelectric materials can be directionally grown by the laser floating zone method (LFZ). It has been determined that the maximum Pb solubility in the textured materials is reached for the 0.4Pb nominal composition. The electrical resistivity data clearly indicated that this Pb amount simultaneously induced the enhancement of metallic behaviour and the reduction of the resistivity. These changes have been explained in terms of hole doping due to Pb^{2+} substitution for Bi^{3+} . The higher power factor value at 300K has been obtained for samples with 0.4Pb nominal content, around $1.0 \cdot 10^{-4} \text{ W/K}^2\text{m}$ (higher than those reported in the

literature for textured specimens), is about two times higher than the obtained for the undoped samples.

Acknowledgements

The authors wish to thank the Gobierno de Aragón (Research Groups T12 and T74), and the Spanish Ministry of Science and Innovation (Project MAT2008-00429) for financial support. The technical contributions of C. Estepa, J. A. Gómez and C. Gallego are also acknowledged.

REFERENCES

- [1] D. M. Rowe: *Thermoelectrics Handbook: Macro to Nano*, ed. D. M. Rowe, CRC Press, Boca Raton, FL., 1st. edn., 2006; pp 1-3.
- [2] I. Terasaki, Y. Sasago, K. Uchinokura, *Phys. Rev. B* 56 (1997) 12685-12687.
- [3] R. Funahashi, I. Matsubara, H. Ikuta, T. Takeuchi, U. Mizutani, S. Sodeoka, *Jpn. J. Appl. Phys.* 39 (2000) L1127-L1129.
- [4] A. C. Masset, C. Michel, A. Maignan, M. Hervieu, O. Toulemonde, F. Studer, B. Raveau, J. Hejtmanek, *Phys. Rev. B* 62 (2000) 166-175.
- [5] H. Leligny, D. Grebille, O. Perez, A. C. Masset, M. Hervieu, B. Raveau, *Acta Cryst. B* 56 (2000) 173-182.
- [6] A. Maignan, D. Pelloquin, S. Hebert, Y. Klein, M. Hervieu, *Bol. Soc. Esp. Ceram. V.* 45 (2006) 122-125.
- [7] A. Maignan, S. Hébert, M. Hervieu, C. Michel, D. Pelloquin, D. Khomskii, *J. Phys.-Condens. Matter* 15 (2003) 2711-2723.
- [8] E. Guilmeau, M. Mikami, R. Funahashi, D. Chateigner, *J. Mater. Res.* 20 (2005) 1002-1008.
- [9] H. Itahara, C. Xia, J. Sugiyama, T. Tani, *J. Mater. Chem.* 14 (2004) 61-66.
- [10] W. Shin, N. Murayama, *J. Mater. Res.* 15 (2000) 382-386.
- [11] A. Sotelo, E. Guilmeau, M. A. Madre, S. Marinel, J. C. Diez, M. Prevel, *J. Eur. Ceram. Soc.* 27 (2007) 3697-3700.
- [12] H.Q. Liu, X.B. Zhao, T.J. Zhu, Y. Song, F.P. Wang, *Current Appl. Phys.* 9 (2009) 409-413.
- [13] M. Kato, Y. Goto, K. Umehara, K. Hirota, I. Terasaki, *Phys. B* 378-380 (2006) 1062-1063.

[14] G. F. de la Fuente, J. C. Diez, L. A. Angurel, J. I. Peña, A. Sotelo, R. Navarro, *Adv. Mater.* 7 (1995) 853-856.

[15] JCPDS chart number 48-0935.

[16] J. Liu, H. S. Yang, Y. S. Chai, L. Zhu, H. Qu, C. H. Sun, H. X. Gao, X. D. Chen, K. Q. Ruan, L. Z. Cao, *Phys. Lett. A* 356 (2006) 85-88.

Table I. Summary of the different contrasts found in SEM micrographs for the as-grown textured samples. For each contrast phase assignment has been based on EDS analysis normalized with respect to Sr (and numbered according to Fig. 4a). Relative amount of each phase in the different samples is also displayed.

Nominal composition	Contrast	Phase composition	Vol. %
$\text{Bi}_2\text{Sr}_2\text{Co}_{1.8}\text{O}_y$	Black (1)	CoO	2.0
	Dark grey (2)	$\text{Sr}_{2.0}\text{Co}_{3.1}\text{O}_y$	8.5
	Grey (3)	$\text{Bi}_{2.7}\text{Sr}_{2.0}\text{Co}_{2.6}\text{O}_y$ (222)	20.0
	Light grey (4)	$\text{Bi}_{2.5}\text{Sr}_{2.0}\text{Co}_{1.1}\text{O}_y$ (221)	68.0
	White (5)	$\text{Bi}_{2.0}\text{SrO}_y$	1.5
$\text{Bi}_{1.8}\text{Pb}_{0.2}\text{Sr}_2\text{Co}_{1.8}\text{O}_y$	Dark grey (2)	$\text{Sr}_{2.0}\text{Co}_{2.8}\text{O}_y$	4.0
	Grey (3)	$\text{Bi}_{1.9}\text{Pb}_{0.2}\text{Sr}_{2.0}\text{Co}_{2.1}\text{O}_y$ (222)	26.0
	Light grey (4)	$\text{Bi}_{2.6}\text{Sr}_{2.0}\text{Co}_{1.3}\text{O}_y$ (221)	68.0
	White (5)	$\text{Bi}_{2.0}\text{SrO}_y$	2.0
$\text{Bi}_{1.6}\text{Pb}_{0.4}\text{Sr}_2\text{Co}_{1.8}\text{O}_y$	Dark grey (2)	$\text{Sr}_{2.0}\text{Co}_{2.6}\text{O}_y$	4.0
	Grey (3)	$\text{Bi}_{2.2}\text{Pb}_{0.5}\text{Sr}_{2.0}\text{Co}_{2.6}\text{O}_y$ (222)	83.0
	White (5)	$\text{Bi}_{1.9}\text{Pb}_{0.3}\text{SrO}_y$	13.0
$\text{Bi}_{1.4}\text{Pb}_{0.6}\text{Sr}_2\text{Co}_{1.8}\text{O}_y$	Dark grey (2)	$\text{Sr}_{2.0}\text{Co}_{2.7}\text{O}_y$	5.0
	Grey (3)	$\text{Bi}_{1.9}\text{Pb}_{0.5}\text{Sr}_{2.0}\text{Co}_{2.2}\text{O}_y$ (222)	76.0
	White (5)	$\text{Bi}_{1.9}\text{Pb}_{0.6}\text{SrO}_y$	19.0

Figure captions

Figure 1. XRD plots of the sintered specimens obtained for the different Pb for Bi substitutions in $\text{Bi}_{2-x}\text{Pb}_x\text{Sr}_2\text{Co}_{1.8}\text{O}_y$. a) 0.0; b) 0.2; c) 0.4; and d) 0.6Pb.

Crystallographic planes have been indicated on the peaks corresponding to the 222 thermoelectric phase. * (Bi,Pb)-Sr-O phase, and # unidentified peaks.

Figure 2. Enlarged view of the (0010) diffraction peaks of $\text{Bi}_{2-x}\text{Pb}_x\text{Sr}_2\text{Co}_{1.8}\text{O}_y$ samples for $x = 0.0; 0.2; 0.4$ and 0.6 , showing their displacement as a function of Pb content. The insert illustrates the relative c -axis variation with respect to the undoped samples.

Figure 3. SEM micrograph of a representative fractured $\text{Bi}_{2-x}\text{Pb}_x\text{Sr}_2\text{Co}_{1.8}\text{O}_y$ sample (for $x = 0.2$), showing the alignment and stacking of the plate-like grains.

Figure 4. SEM micrographs of transversal (a to d) and longitudinal (e to h) polished sections of the $\text{Bi}_{2-x}\text{Pb}_x\text{Sr}_2\text{Co}_{1.8}\text{O}_y$ samples, for $x = 0.0$ (a and e); 0.2 (b and f); 0.4 (c and g); and 0.6 (d and h). The different contrasts are indicated by numbers: 1. CoO (black contrast); 2. Sr-Co-O (dark grey contrast); 3. thermoelectric 222 phase (grey contrast); 4. 221 phase (light grey contrast); and 5. (Bi,Pb)-Sr-O (white contrast).

Figure 5. Temperature dependence of the electrical resistivity, ρ , of $\text{Bi}_{2-x}\text{Pb}_x\text{Sr}_2\text{Co}_{1.8}\text{O}_y$, as a function of the Pb content, x . ● 0.0; ◆ 0.2; ■ 0.4; and ▲ 0.6.

Figure 6. Temperature dependence of the thermopower, S , of

$\text{Bi}_{2-x}\text{Pb}_x\text{Sr}_2\text{Co}_{1.8}\text{O}_y$, as a function of the Pb content, x . ● 0.0; ◆ 0.2; ■ 0.4; and

▲ 0.6.

Figure 7. Temperature dependence of the power factor, PF , of

$\text{Bi}_{2-x}\text{Pb}_x\text{Sr}_2\text{Co}_{1.8}\text{O}_y$, as a function of the Pb content, x . ● 0.0; ◆ 0.2; ■ 0.4; and

▲ 0.6.

Figure 1

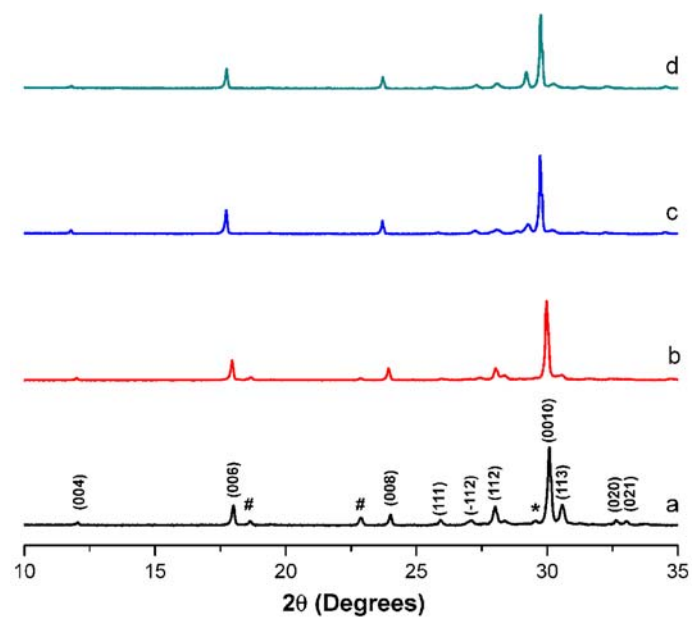


Figure 2

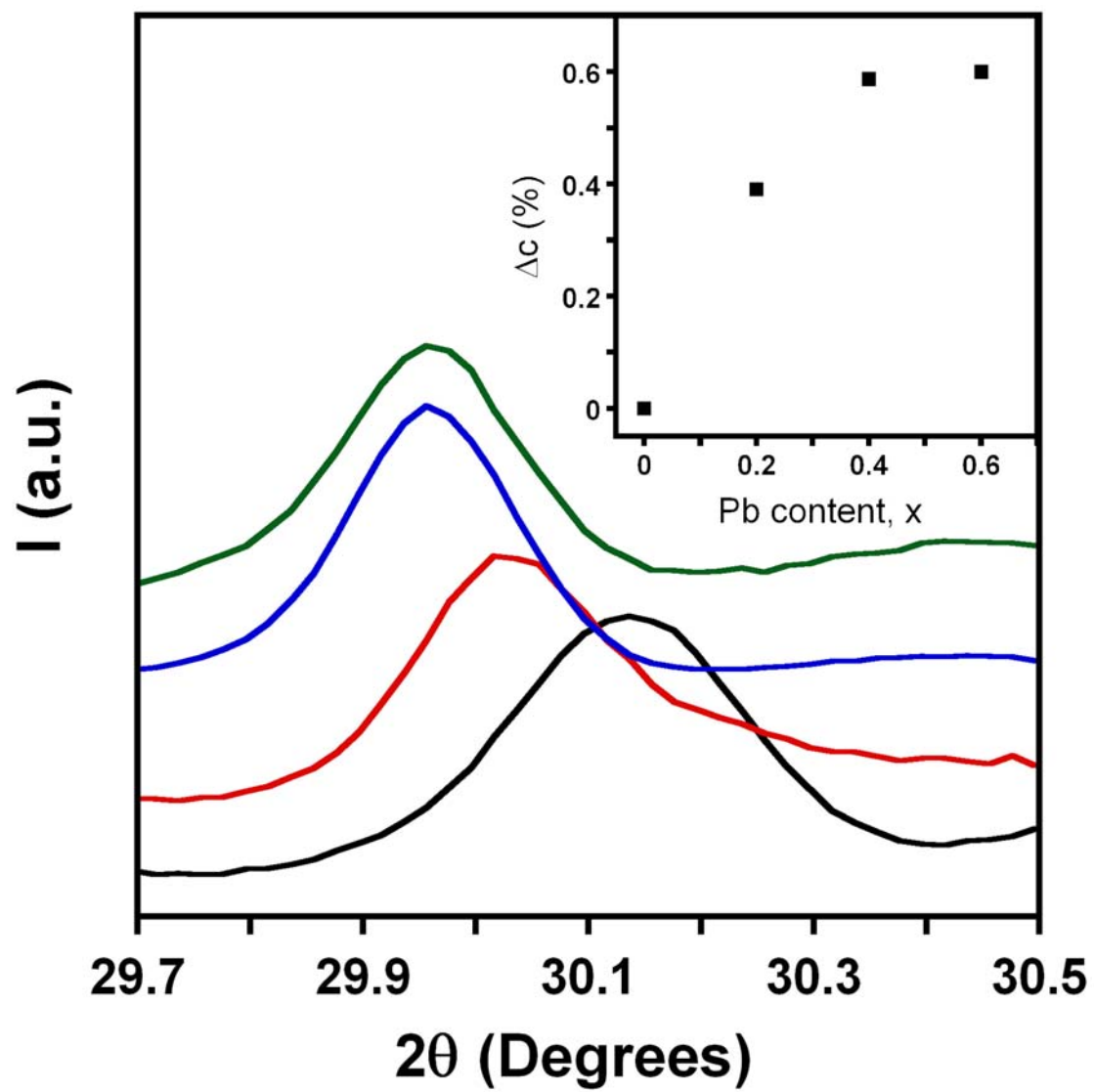


Figure 3

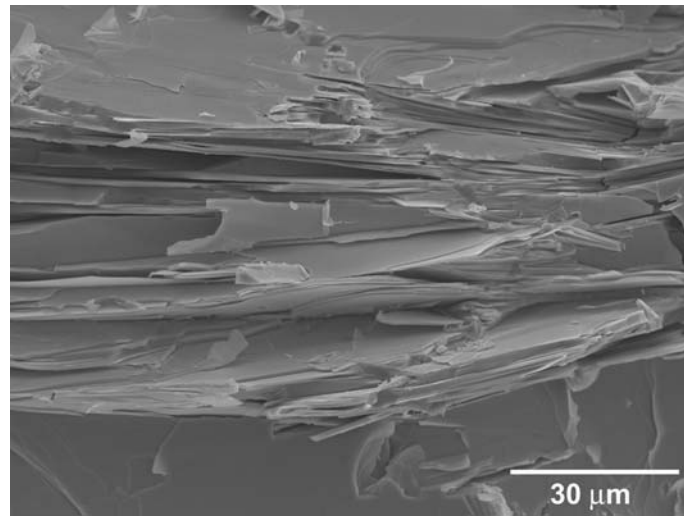


Figure 4

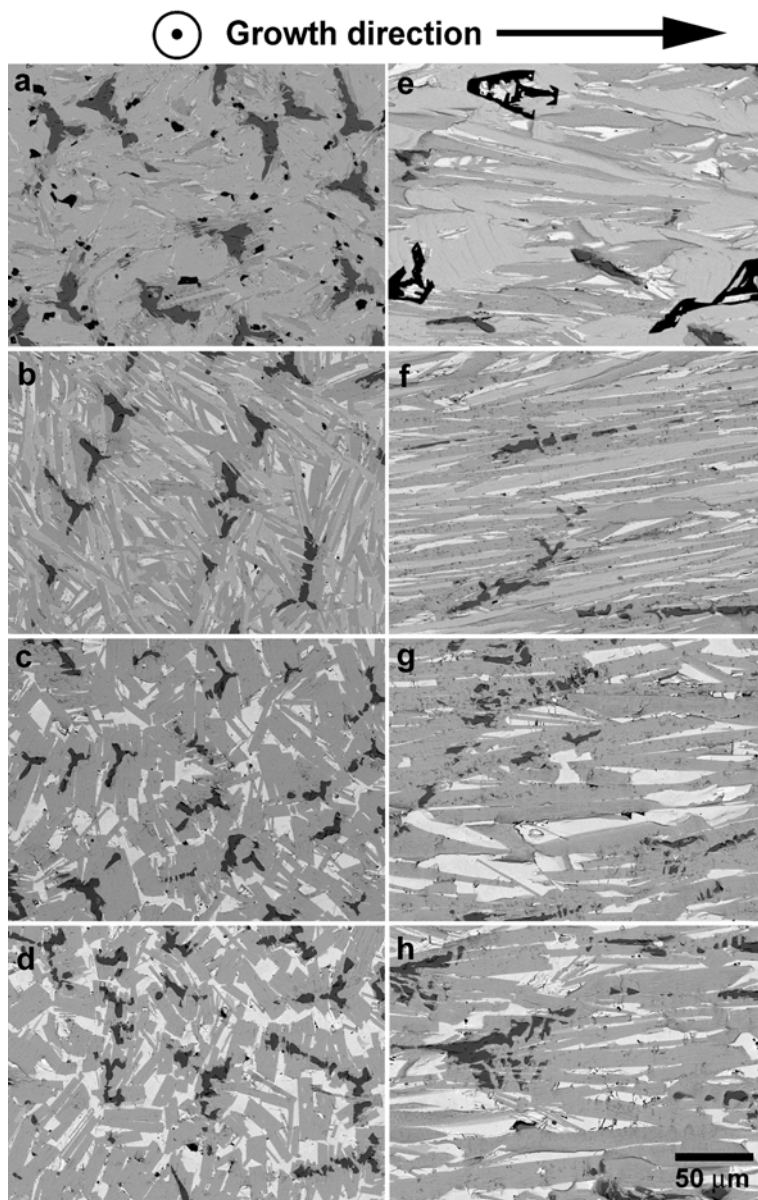


Figure 5

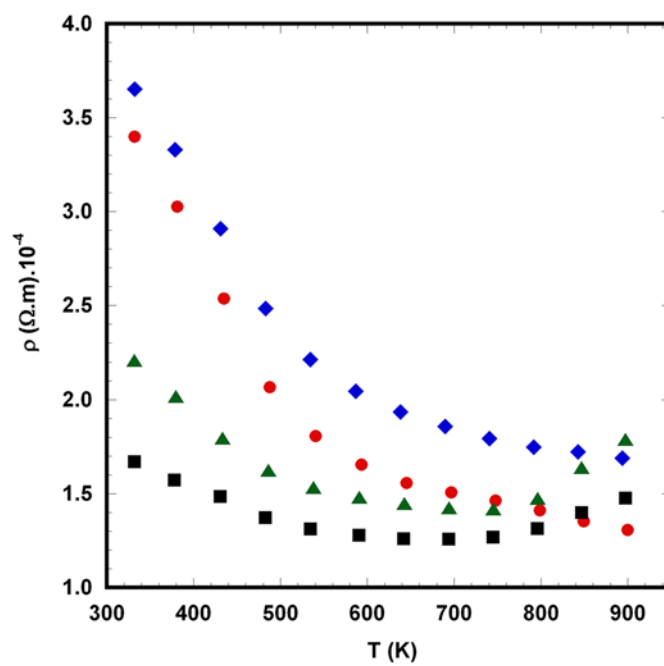


Figure 6

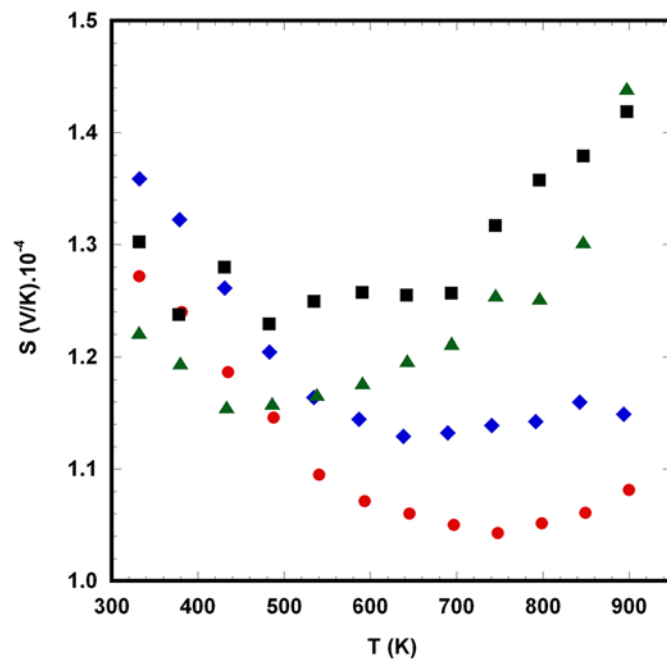


Figure 7

